Metal-Organic Frameworks

Metal Sub-nanoclusters Confined within Hierarchical Porous Carbons with High Oxidation Activity

Xin Zhao, Xiangpeng Kong, Fengliang Wang, Ruiqi Fang,* and Yingwei Li*

Abstract: Metal sub-nanoclusters (SNCs) have shown great promise for a variety of catalytic reactions. However, the fabrication of stable metal SNCs simultaneously with high dispersion and high metal contents remains a challenge. Herein, we report a novel and versatile strategy for the synthesis of various bimetal SNCs stabilized within hierarchical porous carbons (HPC). This facile synthesis only involves the self-assembly of a metal-organic framework (MOF) as the precursor, a molten salt assisted pyrolysis process and the final metal replacement. The metal SNCs (mostly less than 0.8 nm) derived from the metal nodes of the MOF are exclusively confined and homogeneously dispersed throughout the organic ligands derived HPC at high loadings (up to 11.2 wt %). The obtained Cu-Pd@HPC composite exhibits superior catalytic activity and recycling durability in the selective transformation of furfural to maleic acid, achieving 97.8 % yield of maleic acid with a TOF value as high as 20.1 h^{-1} under mild conditions. DFT calculations reveal that the introduction of Pd shifts the partial density of states of Cu toward the Fermi level, leading to stronger chemisorption of furfural to enhance the catalytic activity.

Introduction

Metal species, particularly in the form of metal sub-nanoclusters (SNCs), have sparked intense research interests in heterogeneous catalysis due to their fascinating physico-chemical properties like excellent metal utilization, unique electronic structure and identifiable active sites, which combine the advantages of both homogeneous and hetero-geneous catalysts.[1] Thus, in the last few years, a variety of synthesis methods (e.g., atomic layer deposition,[2] wet impregnation,[3] double-solvent method,[4] and pyrolysis[5]) have been developed for the preparation of metal SNCs immobilized on various porous supports. Whereas, these approaches generally suffer from unwilling metal aggregation

and inhomogeneous nuclearities because of the unpredictable architecture of the precursor and the high free energy of atomic metal species at liquid/thermal environments, result-ing in unsatisfied catalytic performance and stability.

Metal encapsulation has been demonstrated to be highly efficient in enhancing the dispersion and stability of metal SNCs,[6] since the nanoconfinement effect of porous supports towards metal SNCs could suppress them from aggregating or leaching during the synthesis and reaction process.[7] As compared with the conventional porous supports (e.g., mesoporous silicas,[8] zeolites,[9] and carbonous frame-works[10]), metal-organic frameworks (MOFs),[11] a class of emerging coordination polymers featuring intrinsic molecular metal nodes, ordered pores/channels, tunable porosity and easy functionality, exhibit distinctive advantages in the encapsulation of metal SNCs.[12] Noteworthy, apart from being employed as the ideal hosts for the encapsulation of metal SNCs within their bulks, pores, channels or layers, MOFs have also been utilized as versatile pyrolysis precursors to prepare a variety of carbonous derivatives composing of nanoconfined metal SNCs.[13] As an example, Yamamoto et al. developed a DPAG4-TPM template method for the confinement of a series of precisely size-controlled (12 to 60 atoms) noble metal (Ru, Rh, Pd and Pt) sub-nanoclusters within carbonous supports.[14] Li et al. demonstrated the encapsulation of highly dispersed Pd SNCs within derived carbons through a confined thermolysis protocol using Pd-based metal-organic polyhedral as the precursor.[15] Corma et al. reported the confinement of Pt^0_2 clusters within the MOF channels through anchoring K_2PtCl_4 onto the pre-synthesized MOF, i.e., $\{Ca^{II}Cu^{II}_6[(S,S)\text{-methox}]_3(OH)_2\cdot(H_2O)\}\cdot16H_2O)$, with thioether functionalized channels.[16]

Despite of the successes made, it is still difficult to simultaneously achieve the goals of both high metal contents (> 3 wt %) and high dispersion of metal SNCs. Additionally, the porosities of the obtained MOF-based (MOF and MOF-derived) composites are mostly restricted to the microporous regime, which inhibits mass diffusion and hinders the accessibility of the encapsulated metal SNCs. The current pore-extending strategies for the fabrication of meso/macro porous hosts rely heavily on the utilization of costly hard/soft templates and complex operation procedures. In view of these premises, the development of a facile and general protocol to immobilize various metal SNCs within meso- or macroporous supports with high loadings is imperative.

Herein, we demonstrate a versatile molten salt assisted pyrolysis strategy for the encapsulation of bimetal SNCs within hierarchical porous carbons (HPC). The synthesis is facile, which only involves the self-assembly of a MOF template, a pyrolysis process and ultrasound-assisted replace-

[*] X. Zhao, F. Wang, Dr. R. Fang, Prof. Y. Li
State Key Laboratory of Pulp and Paper Engineering, School of Chemistry and Chemical Engineering, South China University of Technology
Guangzhou 510640 (China)
E-mail: fangrq@scut.edu.cn
liyw@scut.edu.cn

X. Kong
The School of Materials Science and Engineering, Harbin Institute of Technology
Shenzhen 518055 (China)

ment. The obtained bimetal SNCs are homogeneously confined in the hierarchical porous carbons with high metal loadings (up to 11.2 wt%). Benefitting from the nanoconfinement effects and synergistic interactions between Cu and Pd species, the as-prepared Cu-Pd@HPC shows unprecedented catalytic performances in furfural (FFA) oxidation, achieving a complete conversion of FFA with 97.8% yield of maleic acid (MA) at 50°C within 4 h in aqueous solution. The turnover frequency (TOF) is as high as $20.1 \, h^{-1}$, outperforming all of the previously reported heterogeneous catalysts under milder or comparable conditions.

Results and Discussion

The synthesis route of Cu-M@HPC (M = Pd, Pt, or Ru) is illustrated in Scheme 1. Firstly, Cu-BDC was self-assembled from $CuSO_4 \cdot 5 H_2O$ and 1,4-benzenedicarboxylic acid (H_2BDC) by using a previously reported solvothermal method.[17] Powder X-ray diffraction (XRD) patterns of the as-synthesized Cu-BDC (Figure S1) matched well with the reported ones. Scanning electron microscopy (SEM) image revealed the three-dimensional polyhedral morphology of Cu-BDC (Figure S2a). In this work, the KCl–KBr mixture, rather than pure KCl or KBr, was selected as the salt for the pyrolysis of Cu-BDC because of its tunable melting points, high stability in a wide temperature range (717–771°C) and mild phase transition process, which offered a relatively stable medium for Cu-BDC decomposition and facilitated the controlling of the pyrolysis process. Typically, the Cu-BDC precursor was mixed with a certain amount of KCl–KBr salt and subjected to pyrolysis under Ar atmosphere. The temperature was set at 730°C, which is higher than both of the decomposition temperature of Cu-BDC (ca. 350°C, as determined by thermal gravity analysis (TGA), Figure S3) and the melting point of the KCl–KBr eutectic composite, i.e., 717°C. After washing with a hydrochloride solution, the Cu@HPC composite was obtained.

SEM and transmission electron microscopy (TEM) images of Cu@HPC revealed that after pyrolysis, the three-dimensional polyhedral Cu-BDC was transformed into hierarchical porous carbons composed of abundant homogeneously distributed macropores in an average size of ca. 120 nm (Figures S2b–d). High-angle annular dark-field scanning TEM (HAADF-STEM) and corresponding elemental mappings suggested the successful immobilization of Cu SNCs throughout the HPC with high dispersion (Figures S2e–h). No significant aggregations were observed even at high Cu loadings (up to 8.6 wt%, as determined by ICP-OES). The valence state of the encapsulated Cu SNCs was identified by X-ray photoelectron spectroscopy (XPS), which showed characteristic peaks of Cu^0 at 932.5 eV and 952.2 eV (Figure 1 f), indicating Cu nodes in Cu-BDC were reduced to Cu^0 after pyrolysis.[18] In the XRD pattern of Cu@HPC (Figure 1a), a broad peak centered at 25.2° was assigned to the (002) plane of graphic carbon species derived from the organic ligands of Cu-BDC, implying the good graphitization degree of the HPC. No characteristic peaks of Cu were detected in Cu@HPC, which was possibly related to their ultrasmall size and high dispersion, in good agreement with the TEM results.

The specific surface areas and porosities of the samples were characterized by nitrogen adsorption at 77 K. Cu@HPC shows a typical type-IV isotherm with a sharp increment in nitrogen uptake at the relative pressure of 0–0.1 and an obvious hysteresis loop (Figure 1 c), revealing the presence of abundant micro- and mesopores within the nanostructure. Besides, the pore-size distribution curves also imply the existence of micro- and mesopores distributed in wide ranges (0.5–1.5 nm and 30–50 nm, respectively) (Figure 1 d). In addition, the nitrogen adsorption isotherm also shows an obviously continuous upward tendency at higher relative pressures ($P/P_0 = 0.95$–1.0), which might be attributed to the formation of macropores. These results suggest the hierarchical porosity of the as-prepared Cu@HPC with micro-, and meso- as well as macropores.
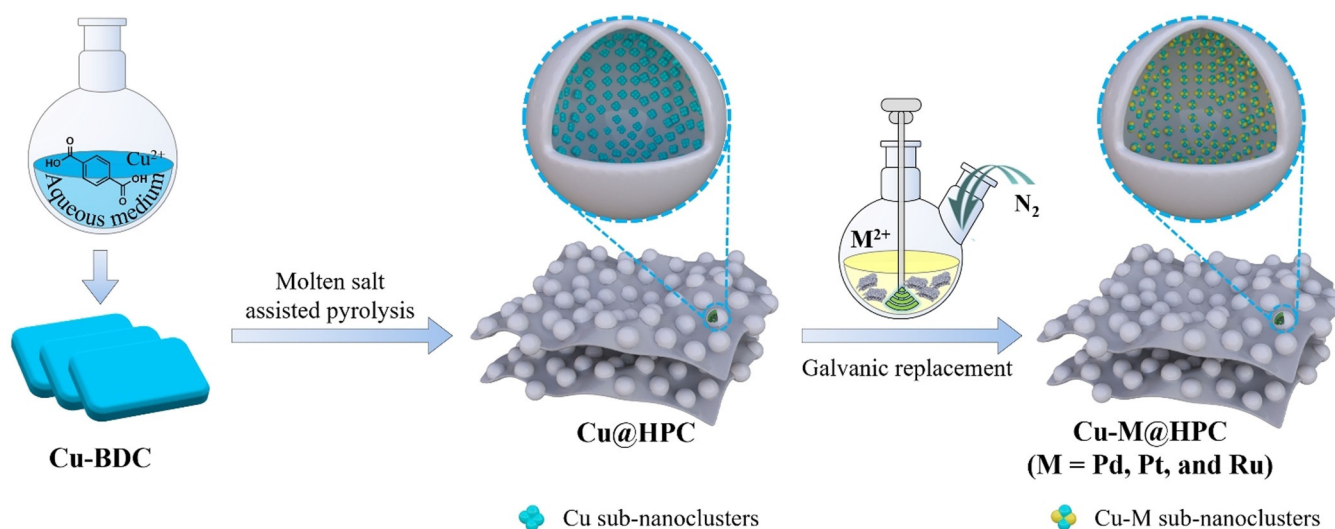
Scheme 1. Schematic illustration of the synthesis process of Cu-M@HPC (M = Pd, Pt, or Ru).
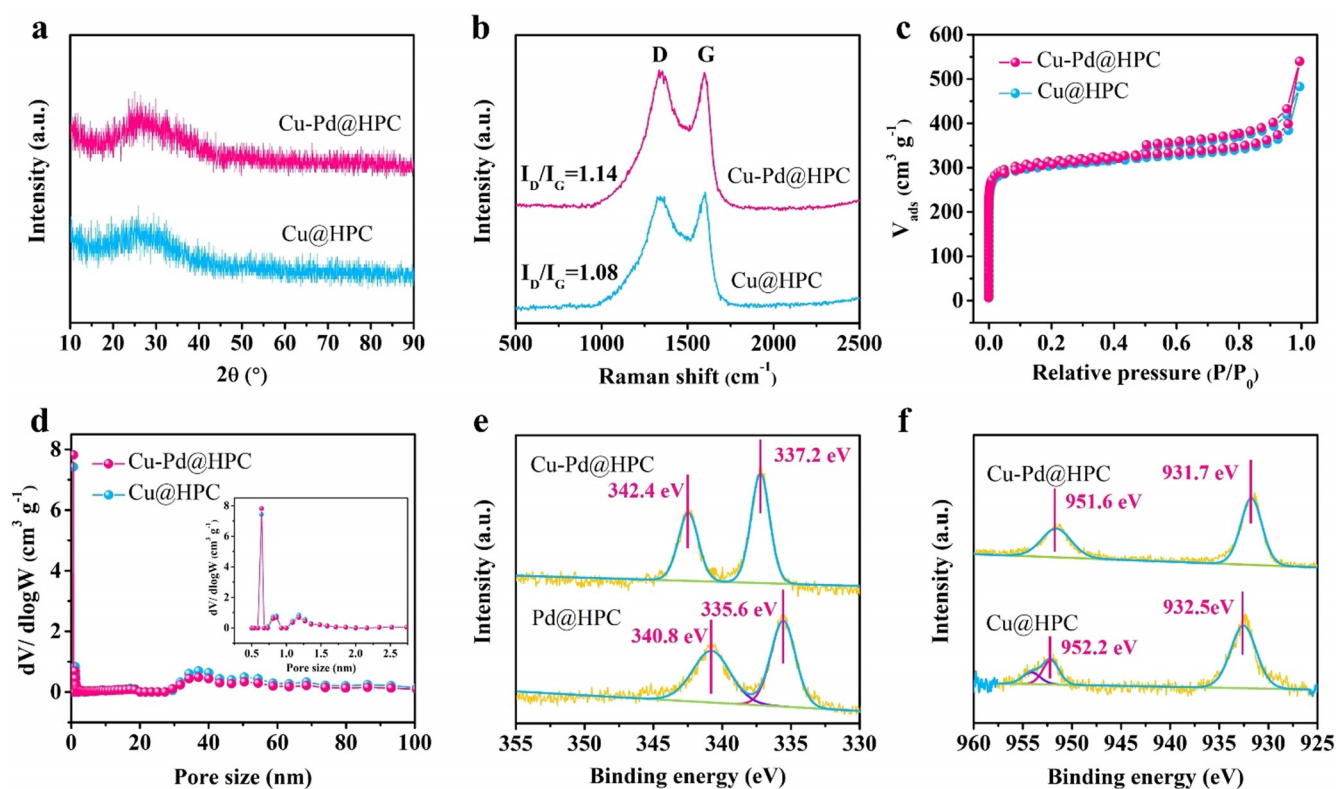
Figure 1. a) XRD patterns, b) Raman spectra, c) N$_2$ adsorption–desorption isotherms, and d) corresponding pore-size distributions of Cu@HPC and Cu-Pd@HPC. e) XPS spectra of Pd 3d region of Pd@HPC and Cu-Pd@HPC, f) XPS spectra of Cu 2p region of Cu@HPC and Cu-Pd@HPC.

Subsequently, Cu@HPC was subject to galvanic replacement in a solution containing Pd^{2+} to partially replace Cu with Pd. The obtained Cu-Pd@HPC inherited the hierarchical porous nanostructure from the parent Cu@HPC with uniformly distributed macropores (Figure 2 a1). Noteworthy, after the galvanic replacement under high-intensity ultrasonic irradiation, the specific surface area and pore volume of the Cu-Pd@HPC were slightly enlarged to 972 m^{2}g^{-1} and 0.63 cm^{3}g^{-1} (Figures 1 c,d and Table S1), respectively, possibly related to the partial removal of Cu species in the micropores. The Cu-Pd SNCs were atomically dispersed (mostly less than 0.8 nm) at a relatively high loading (10.6 wt %) (Figures 2 a1–a3). In addition, the corresponding elemental mappings of C, Cu, and Pd further confirmed the homogeneous distribution of Cu and Pd components without remarkable aggregations (Figures 2 a4–a7). The well-retained broad diffraction peak at 25° in the XRD pattern of Cu-Pd@HPC (Figure 1 a) indicated the preserved graphitization degree. No significant diffractions of Cu or Pd species were detected, which may be due to their ultrasmall sizes and high dispersion. The Raman spectroscopy of Cu-Pd@HPC (Figure 1 b) revealed a slightly increased intensity ratio of the D to G band ($I_D/I_G = 1.14$) as comparison with that of Cu@HPC (1.08), suggesting some defects might be generated after the galvanic replacement.

XPS analysis was carried out on Cu-Pd@HPC to investigate the chemical states of Cu and Pd components and the potential electronic interactions between them (Figures 1 e,f). Two prominent bands located at 342.4 eV and 337.2 eV were

observed in the Pd 3d$_{3/2}$ and Pd 3d$_{5/2}$ regions (Figure 1 e), indicating the existence of Pd$^{\delta+}$ species. The slight shift towards higher binding energy by ca. 1.6 eV in comparison with the metallic Pd was attributed to the interior electron donation phenomena from Pd to Cu atoms.[19] Meanwhile, two bands located at 931.7 eV and 951.6 eV in Cu 2p$_{3/2}$ and Cu 2p$_{1/2}$ regions were assigned to Cu$^{\delta-}$ species (Figure 1 f).[20] There might be some Cu SNCs in the as-prepared Cu-Pd@HPC, but they are hardly identified due to the low content. The negative shift by ca. 0.7 eV in Cu 2p spectrum after the galvanic replacement was also ascribed to the electron transfer phenomenon. The XPS results suggest the successful fabrication of Cu-Pd SNCs with strong metallic synergic effects between the Cu and Pd components.[21]

In view of the above characterization results, it can be concluded that the novel synthesis strategy developed in this work is efficient to fabricate highly dispersed Cu-Pd SNCs confined within hierarchical porous carbons even at a high loading. To examine the versatility of this synthesis approach, Cu-Pt@HPC and Cu-Ru@HPC composites were also prepared under the same conditions except for using Pt and Ru salts as the galvanic replacement precursors (Figures S4 and S5). The obtained Cu-Pt@HPC and Cu-Ru@HPC composites inherited the hierarchical porous structures from the parent Cu@HPC. XPS results revealed the formation of bimetallic Cu-Pt and Cu-Ru SNCs, of which the shift of binding energy suggests their strong synergistic interactions between Cu and Pt/Ru components. TEM and elemental mappings of the Cu-
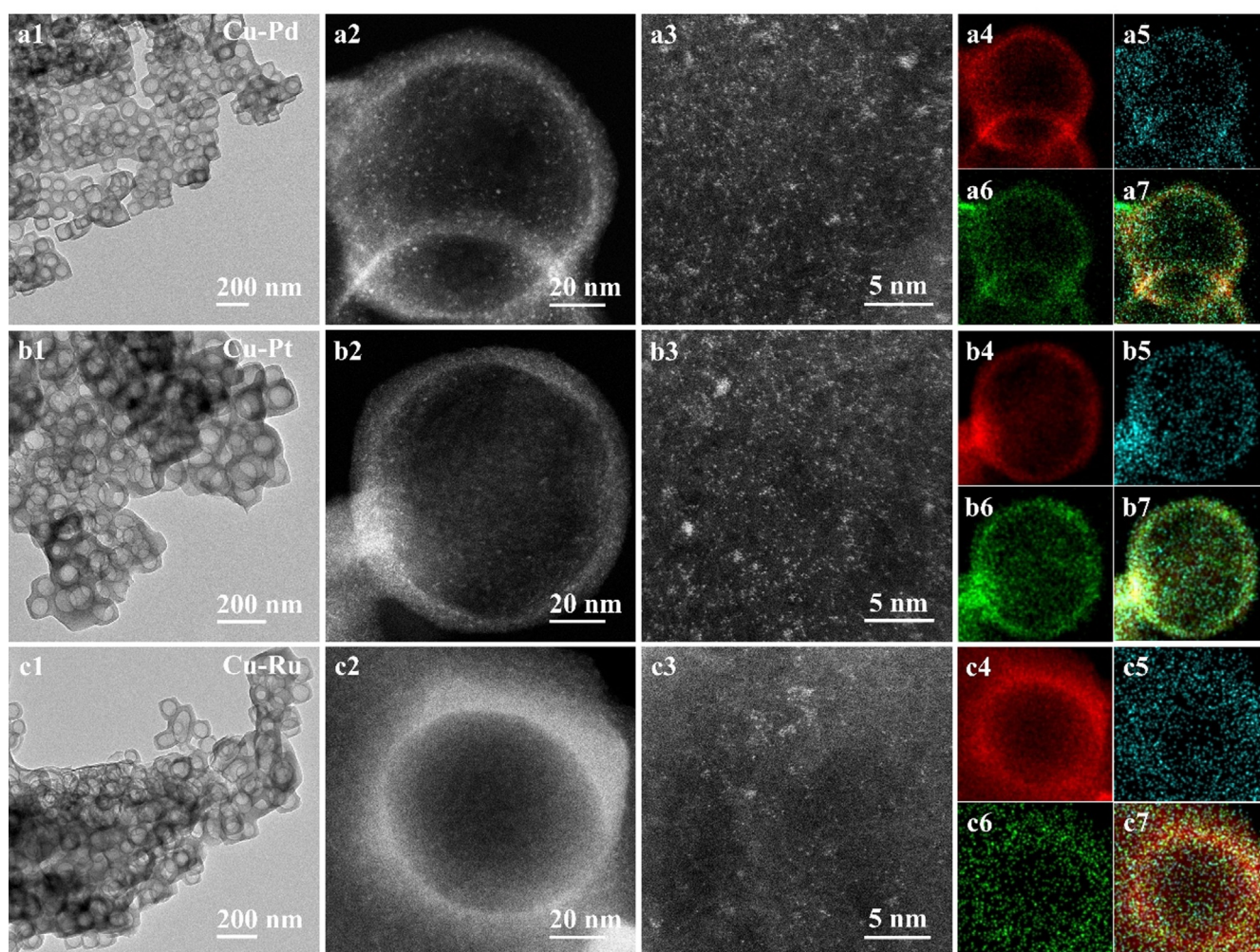
Figure 2. TEM (a1, b1, c1), HAADF-STEM (a2–a3, b2–b3, c2–c3) images, and the corresponding EDX elemental mapping (a4–a7, b4–b7, c4–c7) of C (red), Cu (blue), M (M = Pd, Pt, or Ru, green), and C + Cu + M.

Pt@HPC and Cu-Ru@HPC (Figures 2 b,c) clearly showed the homogeneous encapsulation and high dispersion of the bimetallic Cu-Pt and Cu-Ru SNCs within the hierarchical porous carbons. Also, no significant metal aggregations were observed even at high loadings (11.2 and 9.2 wt% for Cu-Pt and Cu-Ru, respectively).

It is worth to note that the synthesis parameters, including the amount of molten salt, pyrolysis temperature and time are crucial for the preparation of the Cu@HPC composites. In the syntheses, the pyrolysis temperature was selected to be 730 °C. A lower temperature such as 630 °C, was not able to melt KCl–KBr, thus leading to an irregular morphology with negligible macropores (Figure S6a). Otherwise, a higher temperature, e.g., 830 °C or 930 °C, caused uneven macropore distributions and undesired Cu aggregations since the migration of C and Cu species were much more violent under the high temperatures (Figures S6b, S6c). An appropriate loading of molten salt is also significant for this strategy. The use of a small quantity of molten salt only obtained few macropores (Figures S7a, S7b). When the amount of molten salt was increased to 55 equivalents to Cu-BDC, the carbon skeletons collapsed after pyrolysis, probably due to the formation of excessive macropores which underwent subsequent coalescent (Figure S7c). At last, a sufficient pyrolysis time is also of vital importance, either a shorter (1–2 h, Figures S8a, S8b) or longer (5 h, Figure S8c) pyrolysis time resulted in uneven macropore sizes in the obtained HPC.

A plausible mechanism of morphology evolution is proposed to illustrate the formation of the unique hierarchical porous carbons with confined bimetallic SNCs. At 730 °C, the mixed KCl–KBr salt was melt into liquid phase and immediately infiltrated throughout the micropores of Cu-BDC derived composites. The highly concentrated Cl^- and Br^- ions in the molten salt tended to react with Cu^{2+} to form Cu-Cl and Cu-Br complexes, which will be helpful in inhibiting the aggregation of Cu components significantly. Simultaneously, the organic ligands were carbonized to form carbons which inherent microporous nature from the parent Cu-BDC. During the carbonization, the significant loss in weight (Figure S3) and the remarkable decrement in O content (Table S2) suggest the generation and release of a large amount of gases, such as CO_2. As a result, abundant defects

were produced in the obtained carbons, which may serve as the voids for the encapsulation of metal SNCs. According to the Kirkendall effect, the newly formed defects tended to coalesce into micro-, meso- and eventually macropores accompanied with the outwards migration of carbon atoms, which was largely boosted in the liquid-phase molten salt medium. Subsequently, with a drop-in temperature, the KCl–KBr molten salt was precipitated and removed by washing, leaving the Cu SNCs homogeneously encapsulated within the hierarchical carbons consisting of abundant micro-, meso- and macropores. Finally, the nanoconfined Cu-Pd, Cu-Pt and Cu-Ru SNCs were formed upon the galvanic replacement under ultrasonic irradiations. Whereas, in the absence of KCl–KBr, the coalescence process would be too slow to form macropores. On the other hand, the structure of Cu/C might shrink in the subsequent temperature-drop process, which could possibly cause the collapse of the as-formed porous nanostructure. As a result, the as-prepared Cu/C composite featured irregular porous nanostructures without obvious macropores (Figure S9).

The distinctive nano-architectures of Cu-M@HPC stimulate us to investigate their catalytic performances in challenging liquid-phase reactions to obtain value-added chemicals. As we know, maleic acid (MA) is an important reaction intermediate and extensively employed in the manufacture of unsaturated polyester resins, pharmaceuticals and food additives.[22] Unfortunately, the current MA production relies heavily on petroleum-based feedstock.[23] In this regard, the direct oxidation of furfural (FFA), a key platform molecule industrially produced from cellulosic biomass, represents a sustainable route to prepare MA.[24] Thus, in recent years, a variety of catalytic systems have been developed for the oxidation of FFA to MA. However, it remains a big challenge to simultaneously achieve the goals of both high activity and selectivity.[25]

The reactions were carried out at 50 °C and 1 atm air with the presence of H_2O_2. Only 6.5 % MA yield was attained at 32.6 % FFA conversion within 4 h in the absence of any catalyst. For comparison, the Cu/C and Cu-Pd/C materials derived from Cu-BDC were also prepared and employed as the catalysts (Figure S9), which both showed moderate MA yields of 37.6 % and 45.9 % at 67.4 % and 85.5 % FFA conversions, respectively (Figure 3 a). Besides, a series of metallic Cu, Pd and Cu-Pd catalysts on different carbonous supports (e.g., active carbon and graphene, Figures S15,16) were also prepared and employed in this reaction. These catalysts all showed unsatisfied catalytic performances with less than 55 % FFA conversions and 16 % MA yields (Table S4). To our delight, all the Cu-M@HPC composites were highly active for FFA transformation with high turnover frequencies (TOF) (Figure 3 c). Among them, Cu-Pd@HPC exhibited the best catalytic performance with an up to 97.8 % selectivity towards MA at complete conversion (TOF = 20.1 h^{-1}), outperforming all the previously reported heterogeneous catalysts under milder or similar reaction conditions (Table S3). To examine the effect of Cu/Pd molar ratios on their catalytic performances, a series of Cu-Pd@HPC−x (where x represents the molar ratio of Cu/Pd, $x = 0.5$, 1:4, 4:1, and 5:0) catalysts were prepared and also applied in the

FFA oxidation. It can be seen from Figure 3 a that a Cu:Pd molar ratio of 1:1 was optimal to achieve both high activity and high MA selectivity.

The FFA conversion and product selectivity as a function of time over the Cu-Pd@HPC are depicted in Figure 3 d. In view of the reaction results, a plausible reaction pathway for the transformation of FFA to MA over Cu-Pd@HPC is proposed (Figure 3 f). Initially, the FFA molecule undergoes a fast decarbonization-oxidation process to form furan-2(5H)-one (FAO), a highly active compound, which is easily converted into 5-hydroxy-2(5H)-furanone (HFAO). The generated HFAO is oxidized on its -OH group into maleic anhydride (MAN) and finally hydrolyzed to produce MA in the presence of H_2O. Another possible reaction path involves the conversion of FFA to ′FAO, i.e., the isomer of FAO, and the subsequent transformation of ′FAO into succinic acid (SA). Under the investigated reaction conditions, FAO and HFAO were both detected as the intermediates during FFA oxidation over the Cu-Pd@HPC catalyst, whereas the SA yield was only 2.1 %.

Density functional theory (DFT) calculation was conducted to simulate the reaction process and provide theoretical insights to the reaction mechanisms. The densities of state of Cu@HPC, Cu-Pd@HPC, Cu-Pt@HPC, and Cu-Ru@HPC concentrating on the states of d orbitals of Cu were simulated to investigate their electronic properties (Figure 3 e). The Cu-Pd SNCs in Cu-Pd@HPC were electron-rich centers possessing the up-shifted Cu d orbital, which is much closer to the Fermi level in comparison with that of the other three counterparts (Cu-Pt, Cu-Ru and pristine Cu). According to the d band center theory, the Cu-Pd@HPC has much strengthened adsorption towards FFA, which largely contributes to its high catalytic activity.[26] In order to further interpret the excellent MA selectivity of the Cu-Pd@HPC catalyst, periodic DFT calculations were carried out to simulate the adsorption of FAO and ′FAO molecules over the (111) surfaces of Cu-Pd SNCs (Figures 3 f,g and S10, S11). The positive adsorption energies of FAO and ′FAO on Cu (111) facets (0.485 eV and 0.544 eV, respectively) suggest the thermodynamical infeasibility and therefore difficulty in their adsorption under the investigated conditions. In comparison, both FAO and ′FAO exhibited negative adsorption energies over the Cu-Pd (111) facets (−0.236 and −0.105 eV, respectively), implying their spontaneous adsorption on Cu-Pd SNCs. The relatively low adsorption energy of FAO suggests its stronger adsorption over the Cu-Pd (111) facets, which therefore boosted its subsequent transformation into HFAO and finally MA. In view of the facts that the Cu-Pd SNCs possess a suitable adsorption energy towards FAO rather than ′FAO, and they also show a suitable adsorption energy for the intermediate HFAO, it could be understandable that the Cu-Pd SNCs achieved excellent activity and MA selectivity in FFA conversion.

The stability and recyclability of a heterogeneous catalyst are of vital importance for potential applications. Thus, a hot filtration experiment was performed to examine the possible metal leaching during the reaction. As shown in Figure S12a, a slight increment in conversion was observed after filtration, which could be attributed to the fact that oxidation of FFA
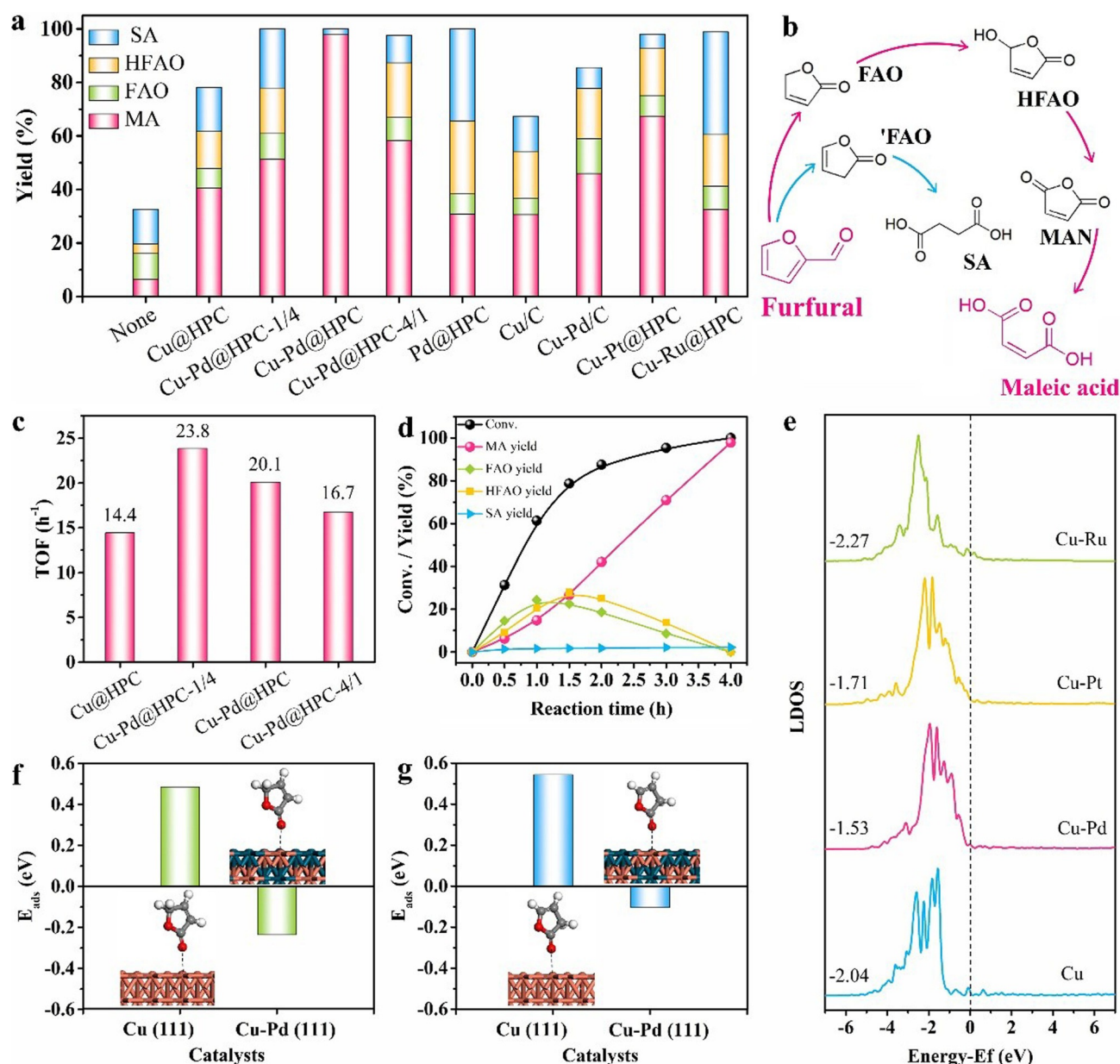
Figure 3. a) Selective oxidation of FFA to MA over different catalysts. Reaction conditions: furfural (1.0 mmol), catalyst (metal 1.25 mol%), H_2O_2 (15 mmol), H_2O (1.5 mL), 50°C, 4 h. Conversion and yield were measured by LC and GC-MS. b) Proposed oxidation route of FFA. c) TOF values for MA production via selective oxidation of FFA over Cu-M@HPC (for detailed information, see Table S3). d) Conversion and yield as a function of time in FFA oxidation over Cu-Pd@HPC. e) The local density of state (LDOS) plots of Cu, Cu-Pd, Cu-Pt, and Cu-Ru. The dashed line stands for the Fermi level. The most favorable configuration and corresponding adsorption energy (E_{ads}) of f) FAO and g) 'FAO on Cu (111) and Cu-Pd (111) simulated by DFT calculations.

can also occur in the absence of any catalyst under the investigated conditions. Moreover, the Cu and Pd contents in the reaction solution were below the detection limit of ICP-OES. These results indicate that the loss of metal active sites was negligible, and the oxidation of FFA was mostly on the heterogeneous surface of Cu-Pd@HPC. After reaction, the catalyst was isolated from the reaction mixture by centrifugation and directly reused after washing with deionized water and ethanol. No obvious activity and selectivity loss were observed in six successive runs (Figure S12b). Furthermore, the morphology, porosity and chemical states of Cu and Pd in

the recycled Cu-Pd@HPC catalyst were all well retained (Figures S13, S14), further confirming the excellent stability and recyclability of the confined Cu-Pd SNCs.

Conclusion

In summary, we have successfully developed a novel and versatile protocol for the efficient encapsulation of metal SNCs within hierarchical porous carbons (HPC). As examples, bimetallic Cu-M SNCs (M = Pd, Pt, or Ru) are exclu-

sively and uniformly confined in the pores of HPC with high loadings. Assessment of the diverse nanostructured catalysts in FFA oxidation confirms the higher catalytic activities of Cu-M@HPC nanocomposites, particularly, the optimized Cu-Pd@HPC exhibits an unprecedented catalytic performance, far outperforming the state-of-art heterogeneous catalysts under similar reaction conditions. More important, no decay in the activity was observed for a number of cycles, suggesting the good stability of the confined metal SNCs. This general strategy for the preparation of high-density and homogeneously dispersed metal SNCs might open a new avenue for the development of highly active metal catalysts for various catalytic applications.

Acknowledgements

Conflict of interest

The authors declare no conflict of interest.

[1] a) E. Tyo, S. Vajda, *Nat. Nanotechnol.* **2015**, *10*, 577–588; b) I. Chakraborty, T. Pradeep, *Chem. Rev.* **2017**, *117*, 8208–8271; c) R. Jin, C. Zeng, M. Zhou, Y. Chen, *Chem. Rev.* **2016**, *116*, 10346–10413; d) J. N. Tiwari, S. Sultan, C. W. Myung, T. Yoon, N. Li, M. Ha, A. M. Harzandi, H. J. Park, D. Y. Kim, S. S. Chandrasekaran, W. G. Lee, V. Vij, H. Kang, T. J. Shin, H. S. Shin, G. Lee, Z. Lee, K. S. Kim, *Nat. Energy* **2018**, *3*, 773–782.

[2] a) X. Liu, S. Jia, M. Yang, Y. Tang, Y. Wen, S. Chu, J. Wang, B. Shan, R. Chen, *Nat. Commun.* **2020**, *11*, 4240–4248; b) C. Liu, B. Yang, E. Tyo, S. Seifert, J. DeBartolo, B. Issendorff, P. Zapol, S. Vajda, L. A. Curtiss, *J. Am. Chem. Soc.* **2015**, *137*, 8676–8679.

[3] X.-K. Wan, H. B. Wu, B. Y. Guan, D. Luan, X. W. Lou, *Adv. Mater.* **2020**, *32*, 1901349.

[4] X. Yang, J.-K. Sun, M. Kitta, H. Pang, Q. Xu, *Nat. Catal.* **2018**, *1*, 214–220.

[5] H. Guan, J. Lin, B. Qiao, X. Yang, L. Li, S. Miao, J. Liu, A. Wang, X. Wang, T. Zhang, *Angew. Chem. Int. Ed.* **2016**, *55*, 2820–2824; *Angew. Chem.* **2016**, *128*, 2870–2874.

[6] a) C. Gao, F. Lyu, Y. Yin, *Chem. Rev.* **2021**, *121*, 834—881; b) L. Chen, R. Luque, Y. Li, *Chem. Soc. Rev.* **2017**, *46*, 4614–4630.

[7] a) R. Fang, P. Tian, X. Yang, R. Luque, Y. Li, *Chem. Sci.* **2018**, *9*, 1854–1859; b) P. Sudarsanam, E. Peeters, E. V. Makshina, V. I. Parvulescub, B. F. Sels, *Chem. Soc. Rev.* **2019**, *48*, 2366–2421.

[8] a) C. Wang, E. Guan, L. Wang, X. Chu, Z. Wu, J. Zhang, Z. Yang, Y. Jiang, L. Zhang, X. Meng, B. C. Gates, F.-S. Xiao, *J. Am. Chem. Soc.* **2019**, *141*, 8482–8488; b) Q. Sun, N. Wang, Q. Bing, R. Si, J. Liu, R. Bai, P. Zhang, M. Jia, J. Yu, *Chem* **2017**, *3*, 477–493.

[9] a) L. Liu, U. Díaz, R. Arenal, G. Agostini, P. Concepción, A. Corma, *Nat. Mater.* **2017**, *16*, 132–138; b) Q. Sun, B. W. J. Chen, N. Wang, Q. He, A. Chang, C.-M. Yang, H. Asakura, T. Tanaka, M. J. Hülsey, C.-H. Wang, J. Yu, N. Yan, *Angew. Chem. Int. Ed.* **2020**, *59*, 20183–20191; *Angew. Chem.* **2020**, *132*, 20358–20366; c) Q. Sun, N. Wang, Q. Fan, L. Zeng, A. Mayoral, S. Miao, R. Yang, Z. Jiang, W. Zhou, J. Zhang, T. Zhang, J. Xu, P. Zhang, J. Cheng, D.-C. Yang, R. Jia, L. Li, Q. Zhang, Y. Wang, O. Terasaki, J. Yu, *Angew. Chem. Int. Ed.* **2020**, *59*, 19450–19459; *Angew. Chem.* **2020**, *132*, 19618–19627.

[10] X. Ao, W. Zhang, Z. Li, J.-G. Li, L. Soule, X. Huang, W.-H. Chiang, H. M. Chen, C. Wang, M. Liu, X. C. Zeng, *ACS Nano* **2019**, *13*, 11853–11862.

[11] a) H. Wang, X. Li, X. Lan, T. Wang, *ACS Catal.* **2018**, *8*, 2121–2128; b) F. R. Fortea-Pérez, M. Mon, J. Ferrando-Soria, M. Boronat, A. Leyva-Pérez, A. Corma, J. M. Herrera, D. Osadchii, J. Gascon, D. Armentano, E. Pardo, *Nat. Mater.* **2017**, *16*, 760–766; c) B. Li, J.-G. Ma, P. Cheng, *Angew. Chem. Int. Ed.* **2018**, *57*, 6834–6837; *Angew. Chem.* **2018**, *130*, 6950–6953; d) C.-J. Liu, N.-N. Zhu, J.-G. Ma, P. Cheng, *Research* **2019**, *9*, 5178573; e) B. Li, J.-G. Ma, P. Cheng, *Small* **2019**, *15*, 1804849.

[12] R. Fang, A. Dhakshinamoorthy, Y. Li, H. Garcia, *Chem. Soc. Rev.* **2020**, *49*, 3638–3687.

[13] a) F. Chen, K. Shen, J. Chen, X. Yang, J. Cui, Y. Li, *ACS Cent. Sci.* **2019**, *5*, 176–185; b) M. Zhao, K. Yuan, Y. Wang, G. Li, J. Guo, L. Gu, W. Hu, H. Zhao, Z. Tang, *Nature* **2016**, *539*, 76–80; c) D. Chen, W. Yang, L. Jiao, L. Li, S.-H. Yu, H.-L. Jiang, *Adv. Mater.* **2020**, *32*, 2000041.

[14] M. Huda, K. Minamisawa, T. Tsukamoto, M. Tanabe, K. Yamamoto, *Angew. Chem. Int. Ed.* **2019**, *58*, 1002–1006; *Angew. Chem.* **2019**, *131*, 1014–1018.

[15] X. Qiu, J. Chen, X. Zou, R. Fang, L. Chen, Z. Chen, K. Shen, Y. Li, *Chem. Sci.* **2018**, *9*, 8962–8968.

[16] M. Mon, M. A. Rivero-Crespo, J. Ferrando-Soria, A. Vidal-Moya, M. Boronat, A. Leyva-Pérez, A. Corma, J. C. Hernández-Garrido, M. López-Haro, J. J. Calvino, G. Ragazzon, A. Credi, D. Armentano, E. Pardo, *Angew. Chem. Int. Ed.* **2018**, *57*, 6186–6191; *Angew. Chem.* **2018**, *130*, 6294–6299.

[17] Z. Sun, F. Xin, C. Cao, C. Zhao, C. Shen, W. Q. Han, *Nanoscale* **2015**, *7*, 20426–20434.

[18] T. Gu, W. Teng, N. Bai, Z. Chen, J. Fan, W. Zhang, D. Zhao, *J. Mater. Chem. A* **2020**, *8*, 9545–9553.

[19] L. Li, W. Yang, Q. Yang, Q. Guan, J. Lu, S.-H. Yu, H.-L. Jiang, *ACS Catal.* **2020**, *10*, 7753–7762.

[20] S. Hu, L. Scudiero, S. Ha, *Electrochim. Acta* **2012**, *83*, 354–358.

[21] S. Bai, Q. Shao, P. Wang, Q. Dai, X. Wang, X. Q. Huang, *J. Am. Chem. Soc.* **2017**, *139*, 6827–6830.

[22] a) H. H. K. Lohbeck, W. Fuhrmann, N. Fedtke, *Ullmann's Encyclopedia of Industrial Chemistry*, Vol. 20, Wiley-VCH, Weinheim, **2000**, pp. 463–473; b) L. A. Badovskaya, L. V. Povarova, *Chem. Heterocycl. Compd.* **2009**, *45*, 1023–1034; c) F. Menegazzo, M. Signoretto, F. Pinna, M. Manzoli, V. Aina, G. Cerrato, F. Boccuzzi, *J. Catal.* **2014**, *309*, 241–247; d) R. M. Contractor, *Chem. Eng. Sci.* **1999**, *54*, 5627–5632; e) R. Wojcieszak, F. Santarelli, S. Paul, F. Dumeignil, F. Cavani, R. V. Gonáalves, *Sustainable Chem. Processes* **2015**, *3*, 9.

[23] a) X.-K. Li, W.-J. Ji, J. Zhao, Z. Zhang, C.-T. Au, *Appl. Catal. A* **2006**, *306*, 8–16; b) X.-K. Li, W.-J. Ji, J. Zhao, Z. Zhang, C.-T. Au, *J. Catal.* **2006**, *238*, 232–241; c) X. Li, J. Ko, Y. Zhang, *ChemSusChem* **2018**, *11*, 612–618; d) R. Mariscal, P. Maireles-Torres, M. Ojeda, I. Sádaba, M. L. Granados, *Energy Environ. Sci.* **2016**, *9*, 1144–1189.

[24] a) D. M. Alonso, J. Q. Bond, J. A. Dumesic, *Green Chem.* **2010**, *12*, 1493–1513; b) M. Stöcker, *Angew. Chem. Int. Ed.* **2008**, *47*, 9200–9211; *Angew. Chem.* **2008**, *120*, 9340–9351; c) D. M. Alonso, S. G. Wettstein, J. A. Dumesic, *Chem. Soc. Rev.* **2012**,

41, 8075–8098; d) R. A. Sheldon, *Green Chem.* **2014**, *16*, 950–963; e) X. Li, P. Jia, T. Wang, *ACS Catal.* **2016**, *6*, 7621–7640.

[25] a) N. Alonso-Fagúndez, M. Ojeda, R. Mariscal, J. L. G. Fierro, M. López Granados, *J. Catal.* **2017**, *348*, 265–275; b) H. Guo, G. Yin, *J. Phys. Chem. C* **2011**, *115*, 17516–17522; c) S. Shi, H. Guo, G. Yin, *Catal. Commun.* **2011**, *12*, 731–733; d) J. Lan, Z. Chen, J. Lin, G. Yin, *Green Chem.* **2014**, *16*, 435–4358.

[26] a) J. K. Nørskov, T. Bligaard, J. Rossmeisl, C. H. Christensen, *Nat. Chem.* **2009**, *1*, 37–46; b) J. R. Kitchin, J. K. Norskov, M. A. Barteau, J. G. Chen, *J. Chem. Phys.* **2004**, *120*, 10240–10246.